

# Coexistence of Different Charge-Transfer Mechanisms in the Hot-Carrier Dynamics of Hybrid Plasmonic Nanomaterials

Jin Zhang,<sup>†,‡,§</sup> Mengxue Guan,<sup>‡,§</sup> Johannes Lischner,<sup>\*,†</sup> Sheng Meng,<sup>\*,‡,§</sup> and Oleg V. Prezhdo<sup>\*,||</sup>

<sup>†</sup>Departments of Materials and Physics and the Thomas Young Centre for Theory and Simulation of Materials, Imperial College London, London SW7 2AZ, United Kingdom

<sup>‡</sup>Beijing National Laboratory for Condensed Matter Physics and Institute of Physics, Chinese Academy of Sciences, Beijing 100190, P.R. China

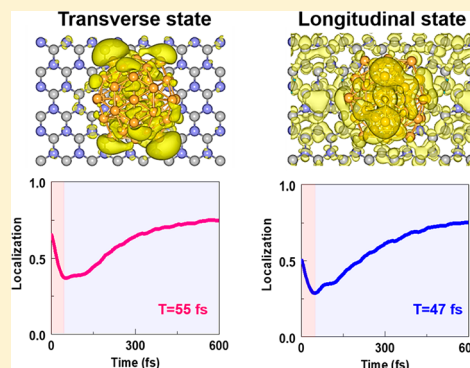
<sup>§</sup>School of Physical Sciences, University of Chinese Academy of Sciences, Beijing 100049, P.R. China

<sup>||</sup>Department of Chemistry, University of Southern California, Los Angeles, California 90089, United States

**S** Supporting Information

**ABSTRACT:** Hot-carrier dynamics at the interfaces of semiconductors and nanoclusters is of significant importance for photovoltaic and photocatalytic applications. Plasmon-driven charge separation processes are considered to be only dependent on the type of donor–acceptor interactions, that is, the conventional hot-electron-transfer mechanism for van der Waals interactions and the plasmon-induced interfacial charge-transfer transition mechanism for chemical bonds. Here, we demonstrate that the two mechanisms can coexist in a nanoparticle–semiconductor hybrid nanomaterial, both leading to faster transfer than carrier relaxation. The origin of the two mechanisms is attributed to the spatial polarization of the excited hot carriers, where the longitudinal state couples to semiconductors more strongly than the transverse state. Our findings provide a new insight into the photoinduced carrier dynamics, which is relevant for many applications in solar energy conversion, including efficient water splitting, photocatalysis, and photovoltaics.

**KEYWORDS:** Two-dimensional heterostructures, charge-transfer mechanisms, plasmonic nanomaterials, interfacial interactions, time-dependent density functional theory



Localized surface plasmons in nanoparticles, coherent quasi-particle excitations of carriers confined to surfaces, have been an active research field in both chemistry and condensed-matter physics for decades.<sup>1–6</sup> Monolayer transition-metal dichalcogenides (TMDs) are promising materials for next-generation ultrathin optoelectronic devices,<sup>7–10</sup> for example, photovoltaic devices, and light detectors, due to their layered structure and excellent semiconducting properties. However, the atomic-scale thickness of TMDs results in relatively low absorbance. One way to overcome this disadvantage is to combine TMDs and small metal clusters to enhance the light–matter interactions due to the unique electronic and optical properties of metal clusters.<sup>11–19</sup> Plasmonic excitations in the metal clusters sensitizing TMDs can lead to hot-carrier transfer from the nanoparticles to the TMDs and electron–hole separation. This is of great interest for many potential applications, including solar energy conversion, efficient water splitting, and light-induced phase transitions.<sup>17–19</sup>

Many experimental and theoretical groups have studied the charge-transfer properties of hybrid materials.<sup>11–34</sup> Wu et al. reported efficient hot-electron transfer induced by a plasmon-induced interfacial charge-transfer excitation at nanoparticle–

semiconductor interfaces.<sup>16</sup> Chen and co-workers revealed that small metal clusters-MoS<sub>2</sub> heterostructures can significantly enhance the hydrogen evolution reactions (compared with pristine TMD).<sup>17</sup> The enhancement was attributed to the injection of photogenerated hot electrons from Au nanorods into MoS<sub>2</sub>. In addition, metal clusters supporting plasmonic hot electrons can induce semiconductor–metal phase transitions in MoS<sub>2</sub> monolayer.<sup>18</sup> Recent pump–probe experiments have tracked ultrafast electron-transfer dynamics from photoexcited gold nanostructures into a MoS<sub>2</sub> monolayer, reporting a time scale of 200 fs.<sup>19</sup> These observations provide a strong motivation for studying microscopic details of charge- and energy-transfer dynamics at the interfaces of small nanoparticles and semiconductors.

To understand the photoinduced processes in plasmonic clusters, Zhang et al. demonstrated that the plasmonic photoexcitation first decays into electron–hole pairs (process I in Figure 1a), and then electrons transfer from nanoparticles to semiconductors (process II), according to the conventional

**Received:** February 13, 2019

**Revised:** April 16, 2019

**Published:** April 17, 2019

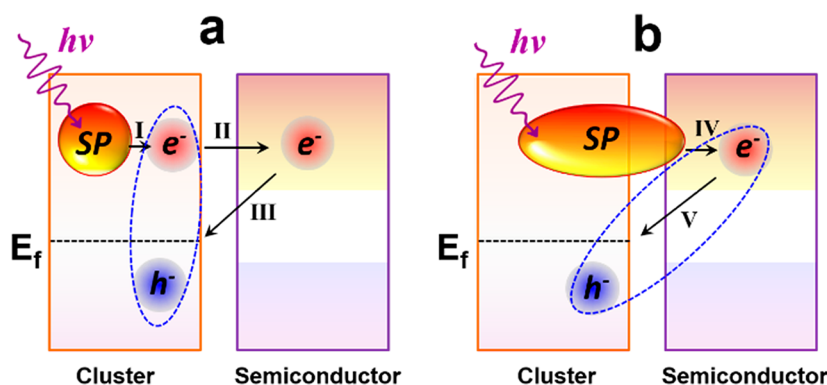


**Figure 1.** Schematics of photoinduced carrier transfer at metal cluster–semiconductor interfaces in energy space. (a) Conventional PHET mechanism. First, surface plasmon (SP) decays into electron–hole pairs and then electrons inject into the semiconductor. Here, I, II, and III indicate plasmon decay, interfacial hot-electron transfer from nanoparticles to semiconductor, and charge diffusion back from semiconductor to cluster, respectively. (b) PICTT mechanism. The plasmonic hot electron has a considerable distribution in the semiconductor upon photoexcitation. IV and V indicate the interfacial hot-electron transfer from cluster to semiconductor and the charge diffusion back from semiconductor to cluster, respectively. The mechanisms in (a) and (b) differ mainly in the delocalization of the photoexcited hot-carrier states between donor and acceptor states.

plasmonic hot-electron-transfer (PHET) mechanism.<sup>32</sup> The injected hot electron can also diffuse back to the metal clusters (process III). Long and Prezhdo<sup>34</sup> proposed an alternative mechanism in which the electron appears inside semiconductors immediately upon photoexcitation with a high probability, that is, plasmon-induced interfacial charge-transfer transition (PICTT) mechanism (process IV in Figure 1b). The instantaneous generation of a charge-separated state upon light illumination rationalizes how plasmon-induced charge transfer can compete with the electron–phonon energy relaxation and charge recombination in metallic particles. Subsequently, the PICTT mechanism was reported in the experiments of Lian and co-workers.<sup>16</sup> The existence of the two mechanisms has been attributed to particle–semiconductor interactions: Chemical bonding leads PICTT, while weak van der Waals (vdW) interactions result in PHET.<sup>32</sup> The crucial question that yet remains to be understood is whether the hot electrons injection from plasmonic metals to semiconductors can compete with the hot-electron relaxation (the cooling process) within the metallic clusters.

In this article, we investigate photon-induced electron injection from small metal clusters ( $\text{Au}_{55}$  and  $\text{Ag}_{55}$ ) into a  $\text{MoS}_2$  monolayer, employing nonadiabatic (NA) molecular dynamics (MD) simulations. We observe a coexistence of the PHET and PICTT mechanisms. The spatial polarization of the excited plasmon plays an important role in the carrier dynamics and can be used to control these novel materials. The competition between the interfacial carrier transfer and energy relaxation is of high importance for the efficiency in the photovoltaic applications. This study paves the way to understand different photoinduced processes induced by photoexcitation in emerging hybrid materials from a new perspective.

The NA MD calculations<sup>35–47</sup> were performed using density functional theory (DFT) as implemented in the Vienna ab initio simulation package using projector-augmented wave (PAW) pseudopotentials in conjunction with the Perdew–Burke–Ernzerhof (PBE) generalized gradient approximation for the exchange–correlation interactions.<sup>48–52</sup> The vdW interactions were included during all calculations at the vdW-DF level with the optB88 exchange functional (optB88-vdW).<sup>53–55</sup> The structure optimization and MD calculations

were performed using only the  $\Gamma$ -point of the first Brillouin zone, with the two in-plane lattice constants ( $6 \times 3\sqrt{3}$  supercell of  $\text{MoS}_2$  unit cells) equal to 19.02 and 16.47 Å, respectively. The model consists of 36 Mo, 72 S, and 55 Au (Ag) atoms. To validate the model, we tested a larger supercell, containing  $6 \times 6\sqrt{3}$   $\text{MoS}_2$  unit cells, to check that no significant artificial interactions between periodic cluster images across the supercell boundary exist. Additional simulation details are provided in Supporting Information (Note S1).

To provide a quantitative description of charge dynamics in the metallic cluster–semiconductor systems, we chose  $\text{Au}_{55}$  and  $\text{Ag}_{55}$  clusters (Figure 2) on the representative two-dimensional (2D)  $\text{MoS}_2$  monolayer. The neutral  $\text{Au}_{55}$  and  $\text{Ag}_{55}$  clusters are open-shell systems with diameters of 1.4 nm. The

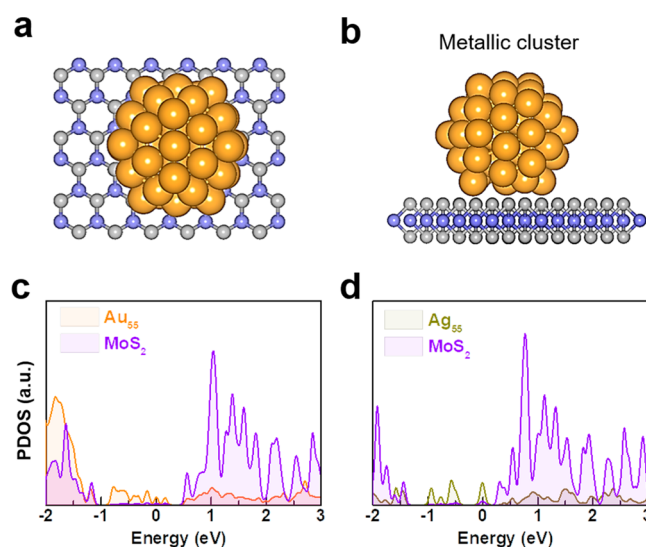


**Figure 2.** Atomic and electronic structures of the nanoparticles/ $\text{MoS}_2$  interfaces. (a) Top and (b) side views of the 55-atom metal cluster on the  $\text{MoS}_2$  monolayer. The orange, blue, and gray balls represent Au, Mo, and S atoms, respectively. PDOS of (c)  $\text{Au}_{55}$  and (d)  $\text{Ag}_{55}$  on a  $\text{MoS}_2$  monolayer. The Fermi levels are set to 0 eV. Purple, orange, and dark yellow curves indicate contributions from  $\text{MoS}_2$ ,  $\text{Au}_{55}$ , and  $\text{Ag}_{55}$ , respectively.

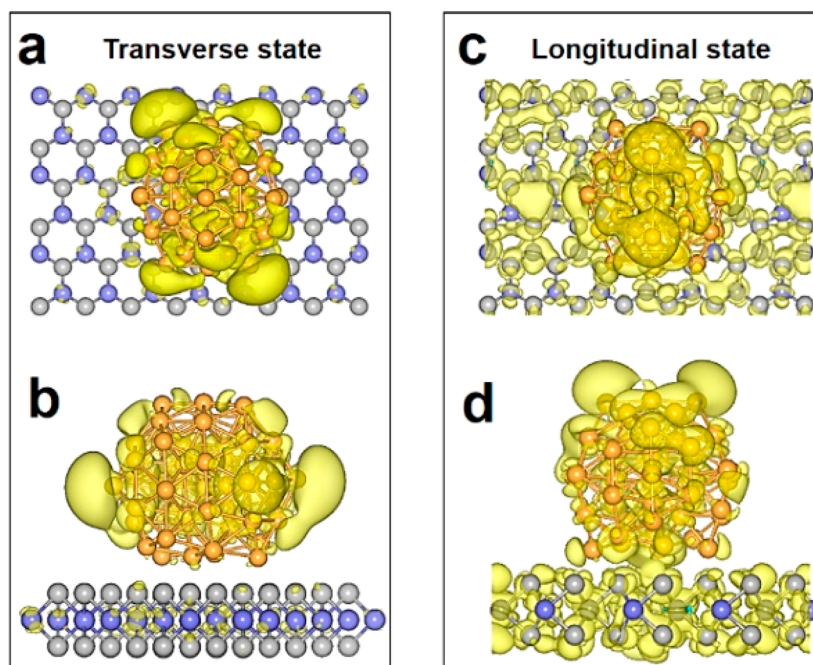


**Figure 3.** Charge distributions of the transverse and longitudinal states for Au<sub>55</sub> on the MoS<sub>2</sub> monolayer. (a) Top and (b) side views of the transverse state, respectively. (c) Top and (d) side views of the longitudinal state, respectively. The longitudinal state has a much larger delocalization between the Au<sub>55</sub> cluster and the MoS<sub>2</sub> monolayer, forming a coherent superposition between the two components. The charge distributions are at the  $1 \times 10^{-3} \text{ e}/\text{\AA}^3$  contour level.

gold and silver nanoclusters have been experimentally synthesized, and their atomic structures have been well determined.<sup>56,57</sup> Most importantly, such small nanoclusters may have excellent potentials for photocatalysis due to high carrier-injection rates.<sup>22</sup> The nearest Au–S atomic distance from the bottom gold atoms to the top sulfur atoms of MoS<sub>2</sub> monolayer is 2.4 Å. The minimum Ag–S distance increases to 2.6 Å for the Ag<sub>55</sub>/MoS<sub>2</sub> heterostructure. During MD simulations, the atomic displacements in the Au<sub>55</sub>/MoS<sub>2</sub> hybrid were larger than those in the Ag<sub>55</sub>/MoS<sub>2</sub> heterostructure, indicating a relatively stronger interfacial interaction. Since MoS<sub>2</sub> has no dangling bonds, the interfacial interactions are weak and arise from vdW forces.

The projected density of states (PDOS) with contributions from metallic clusters and semiconductors are provided in Figure 2. The Fermi levels of the heterostructures lie between the conduction band minimum (CBM) and the valence band maximum (VBM) of MoS<sub>2</sub>. The major difference between Au<sub>55</sub>/MoS<sub>2</sub> (Figure 2c) and Ag<sub>55</sub>/MoS<sub>2</sub> (Figure 2d) is the energy and the extent of state mixing around the CBM of MoS<sub>2</sub>, 0.5 eV for gold cluster and 0.2 eV for silver cluster above the corresponding Fermi levels. The CBM state mixing is much more significant for the Au<sub>55</sub>/MoS<sub>2</sub> heterostructure (see Figure S1). This finding indicates that the Au<sub>55</sub> cluster has a relatively stronger electronic coupling to MoS<sub>2</sub> than the Ag<sub>55</sub> cluster.

To illustrate the accuracy of the PBE functional, we compared the PDOS of Au<sub>55</sub>/MoS<sub>2</sub> calculated using PBE and the hybrid functional HSE06.<sup>58</sup> As shown in Figure S2, we observe that the shape and relative band energies of conduction bands at the PBE level are in consistent with HSE06 calculations. Therefore, PBE functional is good enough to describe photoexcited charge dynamics in this work. Due to the computational complexity of our calculations, which evolve both electron density and vibrational motions explicitly in the

time domain for several picoseconds, involving thousands of nuclear timesteps, and hundreds of thousands of electronic timesteps, we are limited to the current level of description, in particular, to pure-DFT GGA-type functionals, such as PBE.

The spatial distributions of the hot-carrier states in the Au<sub>55</sub>/MoS<sub>2</sub> heterostructure are shown in Figure 3. Additional electronic states are presented in Figure S3. The coupling between the donor and acceptor is directly reflected in the mixing between the corresponding wave functions.<sup>20,32–34</sup> The unoccupied Kohn–Sham orbitals shown in Figure 3 exhibit plasmon-like spatial distributions. Here, the spatial polarization denotes the relative direction between the plasmonic oscillation and the 2D MoS<sub>2</sub> plane. The transverse mode (Figure 3a) indicates that the charge distribution of the plasmonic oscillation is parallel to the MoS<sub>2</sub> monolayer, while the longitudinal mode (Figure 3b) means that the charge distribution of the plasmonic oscillation is perpendicular to the MoS<sub>2</sub> plane. The energies of the two photoexcited modes, computed with the PBE functional, are very similar (2.3 eV for the transverse state versus 2.0 eV for the longitudinal state). We chose the initial states to represent plasmon-like excitations of the Au<sub>55</sub> and Ag<sub>55</sub> clusters based on their energies and charge densities, as illustrated in Figure S3. The interfacial delocalization between the Au<sub>55</sub> cluster and the MoS<sub>2</sub> monolayer differs strongly for the two states. Interestingly, we observe the coexistence of distinct polarization for the plasmon-like modes in the present hybrid nanomaterials, in comparison with the previous studies on a Au<sub>20</sub> pyramid on a TiO<sub>2</sub> surface and a Au<sub>20</sub> pyramid and Au nanorods on the MoS<sub>2</sub> monolayer.<sup>32,33</sup>

To interpret the relationship between surface plasmon-type excitations and Kohn–Sham orbitals, we analyzed excited states of the gold cluster and demonstrated several types of electronic states (see Figures S3–S5). The spatial densities of the photoexcited states in each type in the pristine Au<sub>55</sub> cluster

are displayed in Figure S4. We use charge localization to indicate the fraction the plasmonic excited-state density localized on the nanoclusters. The localization is obtained by integrating the photoexcited electron density over the region of the simulation cell occupied by the Au<sub>55</sub> or Ag<sub>55</sub> cluster (see Supporting Information, Note S1). For instance, a localization = 0.5 means that the photoexcited state is delocalized equally between the nanoparticle and MoS<sub>2</sub>, that is, 50% of the photoexcited state is distributed on the orbitals of the nanoparticle, while the other 50% are on the orbitals of MoS<sub>2</sub>. The states clearly differ in their localization with respect to the gold atoms. The different localizations of these electronic states allow us to classify them approximately as bulk and plasmon-like states. The states delocalized strongly outside of the gold cluster are labeled plasmon-like states, in which hot carriers reside after plasmon excitations.<sup>20</sup> In comparison, the bulk states are almost entirely localized on the gold atoms. The plasmon-like states are not similar to either bulk or surface states, Figure S5. It is important to note that the extensive work, initiated by Schatz and collaborators, and continued by other groups, has demonstrated that atomistic time-dependent DFT (TDDFT) calculations on small metallic particles produce optical excitations corresponding to the plasmonic bands observed experimentally in larger systems.<sup>5,6</sup> Further, we have shown the absorption spectrum obtained from DFT single-particle calculations, Figure S6, where the resulting curve presents a dominant peak at around 2.0 eV, which is significantly lower than the major peak at 3.6 eV obtained from real-time TDDFT simulations.<sup>23</sup> We attribute the underestimation of the plasmonic peak energy obtained at the single-particle level to the PBE exchange–correlation functional, which is known to underestimate excitation energies of semiconductors and clusters. A more accurate description requires explicit consideration of screening and quasiparticle interactions, to account for the self-energy and exciton effects. Such a level of description is too computationally intense for NAMD calculations. The DFT description of the electronic structure is sufficiently accurate to describe the spatial distribution of electronic states and the couplings between them, which are crucial in our dynamic simulations.<sup>36–39</sup> The underestimated plasmonic energies have also been revealed in the Au<sub>20</sub> cluster and Au nanorods, while they are not a dominant factor in the hot-carrier dynamics.<sup>29,30,32,34</sup>

Next, we focus on the photoexcited carrier dynamics for the initial photoexcited states which are mainly distributed on the metal clusters, as captured by the charge-transfer trajectories shown in Figure 4. For the transverse state (Figure 4a), we obtain that the photoexcited state is mainly localized (~65%) on the Au<sub>55</sub> cluster at  $t = 0$  fs. At the initial stage (~50 fs), the localization on the Au<sub>55</sub> cluster decreases rapidly to 35%. This process can be assigned to the hot-electron transfer (process II) after the photoexcited plasmonic state decays into electron–hole pairs (process I) in the conventional PHET mechanism (Figure 1a). Sequentially, it is found that the injected electron transfers back from the MoS<sub>2</sub> monolayer to the Au<sub>55</sub> cluster in 600 fs (process III). The assignments of the multiple processes in Figure 4 are based on the initial states and the time sequences of the photoinduced carrier dynamics following the recent experiments.<sup>16,17</sup> Processes I and II may be entangled in real experiments, or they may be separated in time because process I is too fast (<10 fs) compared to process II (~150 fs). Hot-carrier transfer from the nanoclusters to

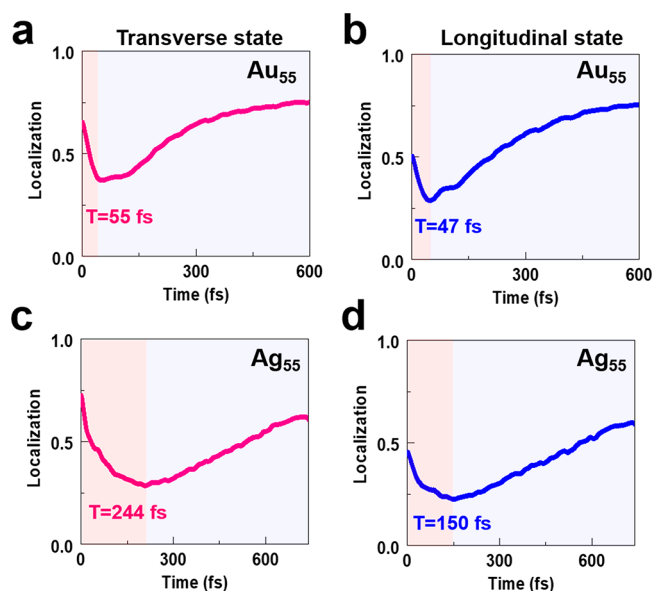


**Figure 4.** Photoexcited plasmonic state dynamics at the Au<sub>55</sub>/MoS<sub>2</sub> and Ag<sub>55</sub>/MoS<sub>2</sub> interfaces. Here, the initial photoexcited states are mainly distributed on the metal clusters. The localization is obtained by integrating the photoexcited electron density over the region of the simulation cell occupied by the Au<sub>55</sub> or Ag<sub>55</sub> cluster. (a) The localization of the hot electron on the Au<sub>55</sub> cluster as a function of time after optical excitation of the transverse state. (b) The localization of the hot electron on the Au<sub>55</sub> cluster after excitation of the longitudinal state. (c) Same as (a) for the Ag<sub>55</sub> cluster. (d) Same as (b) for the Ag<sub>55</sub> cluster.

MoS<sub>2</sub> results in the decay of the localization on Au<sub>55</sub> or Ag<sub>55</sub>, as shown in the light red regimes in Figure 4. For process III, the injected hot carrier on MoS<sub>2</sub> will also have the possibility to diffuse back to Au<sub>55</sub> or Ag<sub>55</sub>, accounting for the increase in the localization on nanoclusters. The crossovers between the decrease regime (in light red) and increase regime (in light blue) are the points when the hot carriers change the transfer direction. Here, we observe a crossover at the time of 55 fs in Figure 4a, indicating a possible reverse pathway from the semiconductor back to the metallic cluster (we will discuss the process in detail next). The longitudinal state (Figure 4b) follows a similar trend with the crossover at 47 fs (process IV in the PICTT mechanism, Figure 1b), faster than the transverse state. Notably, both time scales are faster than the time scale of energy relaxation inside the Au<sub>55</sub> cluster (~500 fs, Figure S7).

For the silver cluster on MoS<sub>2</sub>, the hot-electron transfer takes place in 244 fs for the transverse state, whereas it takes 150 fs for the longitudinal state. We note the hot-electron state in the Ag<sub>55</sub> cluster relaxes to the band edge on a longer time scale (several picoseconds), validating the generality of ultrafast interfacial charge transfer. Therefore, we come to another important finding of this work: The spatial polarization of excited states is a crucial factor for the photoexcited charge dynamics at interfaces of metallic clusters and semiconductors.

We further analyze the hot-carrier-transfer process from MoS<sub>2</sub> to the metallic clusters for the initial photoexcited states that are mainly localized on the MoS<sub>2</sub> monolayer. The localizations and energies of the transferred hot electrons in MoS<sub>2</sub> are monitored, as displayed in Figure 5. For the gold cluster on MoS<sub>2</sub>, the hot electron transfers back to Au<sub>55</sub> in 230

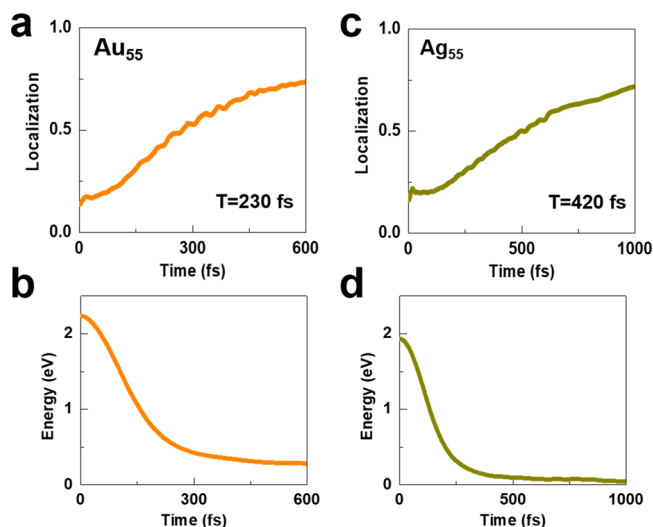


**Figure 5.** Hot-electron transfer from MoS<sub>2</sub> to the metallic clusters. Here, the initial photoexcited states are mainly localized on the MoS<sub>2</sub> monolayer. (a) Localization of the excited hot electron on the Au<sub>55</sub> cluster as a function of time. (b) The electronic excitation energy evolution of hot electrons for the Au<sub>55</sub>/MoS<sub>2</sub> system. (c) Localization of the excited hot electron on the Ag<sub>55</sub> cluster with the initial photoexcited state mainly localized on MoS<sub>2</sub>. (d) The electronic excitation energy evolution of hot electrons in the Ag<sub>55</sub>/MoS<sub>2</sub> system.

fs. The process for the silver cluster takes place in 420 fs, slower than for the gold cluster on MoS<sub>2</sub>. This can be attributed to the interfacial coupling strength between the metallic cluster and the semiconductor. Particularly, the states at CBM of the Au<sub>55</sub> and Ag<sub>55</sub> clusters on MoS<sub>2</sub> exhibit a significant difference, the spatial delocalization for the Au<sub>55</sub> cluster on MoS<sub>2</sub> is much larger than that of the Ag<sub>55</sub> cluster on MoS<sub>2</sub>. However, both time scales are smaller than the hot-electron relaxation process within the MoS<sub>2</sub> monolayer ( $\sim 600$  fs).<sup>26</sup> This demonstrates that the injected hot carriers in the MoS<sub>2</sub> monolayer can transfer back to the metallic clusters before electron–hole recombination inside MoS<sub>2</sub> that occurs on a much longer time scale ( $\sim 500$  ps), as explored by Li et al.<sup>59</sup> We note the hot-electron relaxation process in TMDs can be influenced by many factors, including defects and interfacial strains. Zhang and co-authors have demonstrated that sulfur defects or trap states can accelerate the relaxation process to  $\sim 200$  fs for the MoS<sub>2</sub> monolayer.<sup>26</sup> Therefore, we deduce the process of hot-carrier reverse transfer is sensitive to the quality of samples in experiments and interfacial interactions in different heterostructures. It should be noted that the energy in Figure 5 is not the Kohn–Sham energy of one specific state. It is calculated by averaging the electronic energy over time-dependent populations of multiple electronic states as well as over initial configurations and realizations of the surface hopping trajectories (see Supporting Information, Note S1, for more details).

To further understand the mechanisms of photoexcited-state dynamics, we analyze the effects of phonons, as exhibited in Figure 6. Vibrational motions can accelerate charge dynamics and are responsible for energy losses to heat because the electron–phonon interaction provides crucial channels for hot-electron relaxation.<sup>48–52</sup> The normalized energy gap autocorrelation function (ACF) of the photoexcited state exhibits how the energy at a specific time depends on its previous values. We present the normalized autocorrelation functions of the

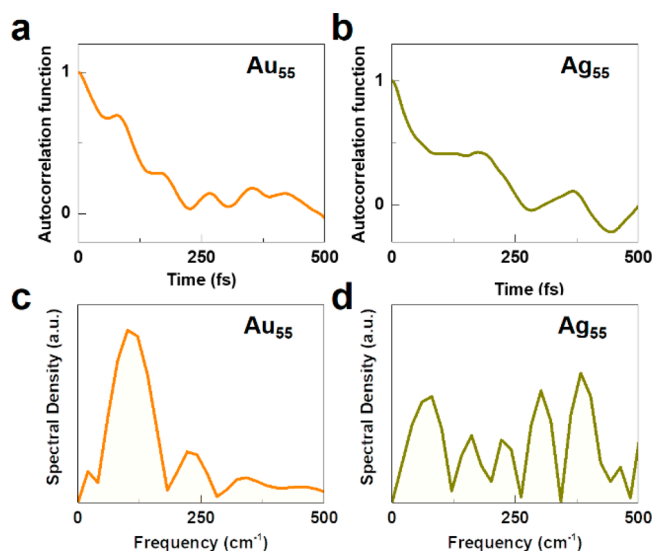


**Figure 6.** Phonon effect in charge dynamics. (a) Autocorrelation functions of the photoexcited state for the transverse mode with an energy of 2.3 eV in the Au<sub>55</sub>/MoS<sub>2</sub> heterostructure. (b) Autocorrelation functions of the photoexcited state for the transverse mode with an energy of 2.0 eV in the Ag<sub>55</sub>/MoS<sub>2</sub> heterostructure. (c) Spectral density of the phonon modes for the Au<sub>55</sub>/MoS<sub>2</sub> heterostructure. (d) Same as (c) for the Ag<sub>55</sub>/MoS<sub>2</sub> heterostructure.

photoexcited states (the transverse and longitudinal modes) in the two hybrid heterostructures in Figure 6a,b. In the Au<sub>55</sub>/MoS<sub>2</sub> hybrid, the normalized ACF decreases from 1 to 0 within 200 fs, followed by a slight oscillation. In comparison, the normalized ACF for the Ag<sub>55</sub>/MoS<sub>2</sub> hybrid decreases rapidly to 0 in 270 fs and oscillates significantly with a dominant period of  $\sim 150$  fs. The oscillation amplitude reaches 40% of the initial value, reflecting that the memory of the energy fluctuation extends into several hundred femtoseconds.

More information comes from the spectral densities, that is, Fourier transformation of the photoexcited-state energies (transverse and longitudinal states) along the MD (see Supporting Information, Note S1). For the Au<sub>55</sub>/MoS<sub>2</sub> hybrid, the 100 cm<sup>-1</sup> mode shows the largest amplitude and contributes most to NA electron–phonon coupling in gold clusters.<sup>32,34</sup> It reveals that surface plasmons couple exclusively to low-frequency vibrational modes of gold (Figure 6c,d). In the Ag<sub>55</sub>/MoS<sub>2</sub> heterostructure, the mode at 100 cm<sup>-1</sup> has a relatively small amplitude, and the Raman active A<sub>1g</sub> mode of MoS<sub>2</sub> at  $\sim 400$  cm<sup>-1</sup> is also crucial in the dynamics.<sup>59–61</sup> It is not surprising that phonon modes of both MoS<sub>2</sub> and metallic clusters are involved in the hot-electron relaxation. This observation elucidates the novel hot–electron decaying channels, contributing to our understanding of the coexistence of the PHET and PICTT mechanisms in weakly bound photoelectric hybrids.

To confirm the model, we performed additional tests by changing the shape and size of supercell (see Figures S8–S10). We use a larger rhomboidal-shaped supercell containing  $6 \times 6$  MoS<sub>2</sub> unit cells, and a larger rectangular supercell containing  $6 \times 6\sqrt{3}$  MoS<sub>2</sub> unit cells. Comparison of the charge densities of the plasmon-like states shown in Figures 3 and S8 demonstrates that the shape of the simulation cell does not influence the density distribution. The charge-transfer dynamics simulated using the larger rectangular supercell and rhomboid supercell (Figures S8–S9) are almost identical to

those in the main text. In particular, the plasmon-driven hot-electron transfer from the Au<sub>55</sub> cluster to MoS<sub>2</sub> requires around 50 fs in both cases. Both charge injection and relaxation dynamics are slightly faster in the larger simulation cell due to a higher density of states in MoS<sub>2</sub> and additional phonon modes available in the larger MoS<sub>2</sub> layer. Therefore, our model is sufficiently accurate to describe the carrier dynamics. The determined time scales and mechanisms are dependent primarily on the interfacial interactions between the metallic clusters and MoS<sub>2</sub>.

Several theoretical groups have investigated photoexcited carrier dynamics in materials involving plasmonic hot electrons.<sup>1,22–26</sup> Brongersma et al. demonstrated how plasmon excitations in metallic nanostructures allow for the generation and utilization of plasmon-induced hot carriers, offering exciting opportunities for fundamental research and applications.<sup>1</sup> Atwater and co-authors reported that plasmon-generated hot-carrier distributions are sensitive to the electronic band structure.<sup>22</sup> Brown et al. have investigated nonradiative plasmon decay mechanisms and hot-carrier dynamics, considering the effects of phonons, surfaces, and geometry.<sup>25</sup> They combined first-principles electronic structure calculations, harmonic phonon approximation, and second-order perturbation theory to obtain electron–phonon matrix elements and compute phonon-assisted transition rates, characterizing intrinsic lifetimes of electronic states as an additional source of plasmon loss. Their method captures the microscopic mechanisms underlying surface plasmon decay.<sup>25</sup>

In the experiments, Wu et al. studied the plasmon-induced interfacial charge-transfer pathway in quantum-confined semiconductor–Au nanorod heterostructures.<sup>16</sup> Strong interfacial interactions resulted in a strong damping of the plasmon band in the Au tip. The proposed pathway was verified by observing highly efficient plasmon-induced Au-to-semiconductor charge separation with high quantum efficiencies upon excitation. They also observed plasmon-induced hot-electron transfer from the Au cluster to the semiconductor with a time scale of ~20 fs. Such an ultrafast charge separation time is consistent with the PICTT mechanism studied in this work. In addition, Yu and co-authors have studied electron transfer from Au nanorods to MoS<sub>2</sub>.<sup>18</sup> They observed that plasmons can decay and generate hot electrons within the first few femtoseconds, followed by hot-electron transfer which occurs within 200 fs, in good agreement with the conventional PHET mechanism. It should be noted that the gold and silver clusters studied in the work are quite small (~1.4 nm). For more complex systems (e.g., core–shell quantum clusters with larger sizes),<sup>31</sup> the orientation of the clusters relative to the substrate and the polarization of plasmonic hot states should be considered carefully.

Based on the simulations, we propose a new physical picture in hybrid plasmonic nanomaterials. Beyond the intrinsic type of interfacial interactions (chemical bonds and vdW couplings), the polarization direction of the plasmonic excited states (i.e., the relative direction between the plasmonic modes and the MoS<sub>2</sub> plane) is crucial and accounts for the coexistence of different charge-transfer mechanisms, both leading to faster transfer than carrier relaxation. These findings are not only consistent with the experimentally observed interlayer electron transfer in small metal cluster–TMDs heterostructures but also provide an understanding of the ultrafast charge dynamics in nanoparticle–semiconductor heterostructures.

To conclude, we studied the photoexcited hot-carrier dynamics in the hybrid nanomaterials. Our results indicated coexistence of the PHET and PICTT mechanisms for photoexcitation-driven charge separation in hybrid plasmonic nanomaterials. Furthermore, the polarization of the excited states in metallic clusters is of significant importance for hot-electron dynamics at the interfaces between nanoparticles and semiconductors. In addition, we found that the injected hot carriers in semiconductors can transfer back to metallic clusters through interlayer hopping. The above findings provide a new perspective for hot-electron dynamics in hybrid nanomaterials for designing potential devices based on light-absorption materials.

## ■ ASSOCIATED CONTENT

### Supporting Information

The Supporting Information is available free of charge on the ACS Publications website at DOI: 10.1021/acs.nanolett.9b00647.

Detailed analysis of states in the metal clusters and hybrid heterostructures and more details on the methods (Figures S1–S10 and Note S1) (PDF)

## ■ AUTHOR INFORMATION

### Corresponding Authors

\*E-mail: prezhd@usc.edu.

\*E-mail: smeng@iphy.ac.cn.

\*E-mail: j.lischner@imperial.ac.uk.

### ORCID

Jin Zhang: 0000-0001-7830-3464

Sheng Meng: 0000-0002-1553-1432

Oleg V. Prezhdo: 0000-0002-5140-7500

### Notes

The authors declare no competing financial interest.

## ■ ACKNOWLEDGMENTS

This work was supported by the National Key Research and Development Program of China (grant nos. 2016YFA0300902 and 2015CB921001), National Natural Science Foundation of China (grant nos. 11774396 and 11474328), and “Strategic Priority Research Program (B)” of Chinese Academy of Sciences (grant no. XDB07030100). O.V.P. acknowledges financial support from the U.S. Department of Energy, grant DE-SC0014429. J.Z. acknowledges funding through the Royal Society Global Challenges Grant CHG\R1\170063. J.Z. thanks Lei Yan and Huixia Fu for helpful discussions.

## ■ REFERENCES

- (1) Brongersma, M. L.; Halas, N. J.; Nordlander, P. *Nat. Nanotechnol.* **2015**, *10*, 25–34.
- (2) Lincic, S.; Christopher, P.; Ingram, D. B. *Nat. Mater.* **2011**, *10*, 911–921.
- (3) Klar, T.; Perner, M.; Grosse, S.; von Plessen, G.; Spirkl, W.; Feldmann, J. *Phys. Rev. Lett.* **1998**, *80*, 4249–4252.
- (4) Jin, R.; Cao, Y. C.; Hao, E.; Métraux, G. S.; Schatz, G. C.; Mirkin, C. A. *Nature* **2003**, *425*, 487.
- (5) Jensen, L.; Aikens, C. M.; Schatz, G. C. *Chem. Soc. Rev.* **2008**, *37*, 1061–1073.
- (6) Zhao, L.; Jensen, L.; Schatz, G. C. *J. Am. Chem. Soc.* **2006**, *128*, 2911–2919.
- (7) Chhowalla, M.; Shin, H. S.; Eda, G.; Li, L. J.; Loh, K. P.; Zhang, H. T. *Nat. Chem.* **2013**, *5*, 263–275.

- (8) Yu, W. J.; Liu, Y.; Zhou, H. L.; Yin, A. X.; Li, Z.; Huang, Y.; Duan, X. F. *Nat. Nanotechnol.* **2013**, *8*, 952–958.
- (9) Boulesbaa, A.; Wang, K.; Mahjouri-Samani, M.; Tian, M.; Puzetzy, A. A.; Ivanov, I.; Rouleau, C. M.; Xiao, K.; Sumpster, B. G.; Geohegan, D. B. *J. Am. Chem. Soc.* **2016**, *138*, 14713–14719.
- (10) Amani, M.; Lien, D. H.; Kiriya, D.; Xiao, J.; Azcatl, A.; Noh, J.; Madhvapathy, S. R.; Addou, R.; Kc, S.; Dubey, M.; Cho, K.; Wallace, R.; Lee, S.; He, J.; Ager, J. W.; Zhang, X.; Yablonovitch, E.; Javey, A. N. *Science* **2015**, *350*, 1065–1068.
- (11) Wen, X.; Xu, W.; Zhao, W.; Khurgin, J. B.; Xiong, Q. *Nano Lett.* **2018**, *18*, 1686–1692.
- (12) Lee, K. C.; Chen, Y. H.; Lin, H. Y.; Cheng, C. C.; Chen, P. Y.; Wu, T. Y.; Shih, M. H.; Wei, K. H.; Li, L. J.; Chang, C. W. *Sci. Rep.* **2015**, *5*, 16374–16382.
- (13) Forcherio, G. T.; Roper, D. K. *Adv. Opt. Mater.* **2016**, *4*, 1288–1294.
- (14) Liu, W.; Lee, B.; Naylor, C. H.; Ee, H. S.; Park, J.; Johnson, A. T.; Agarwal, R. *Nano Lett.* **2016**, *16*, 1262–1269.
- (15) Tisdale, W. A.; Williams, K. J.; Timp, B. A.; Norris, D. J.; Aydil, E. S.; Zhu, X. Y. *Science* **2010**, *328*, 1543–1547.
- (16) Wu, K. F.; Chen, J.; McBride, J. R.; Lian, T. *Science* **2015**, *349*, 632–635.
- (17) Shi, Y.; Wang, J.; Wang, C.; Zhai, T. T.; Bao, W. J.; Xu, J. J.; Xia, X. H.; Chen, H. Y. *J. Am. Chem. Soc.* **2015**, *137*, 7365–7370.
- (18) Yu, Y.; Ji, Z.; Zu, S.; Du, B.; Kang, Y.; Li, Z.; Zhou, Z.; Shi, K.; Fang, Z. *Adv. Funct. Mater.* **2016**, *26*, 6394–6401.
- (19) Kang, Y.; Najmaei, S.; Liu, Z.; Bao, Y.; Wang, Y.; Zhu, X.; Halas, N. J.; Nordlander, P.; Ajayan, P. M.; Lou, J.; Fang, Z. *Adv. Mater.* **2014**, *26*, 6467–6471.
- (20) Guo, Z. Y.; Habenicht, B. F.; Liang, W. Z.; Prezhdo, O. V. *Phys. Rev. B: Condens. Matter Mater. Phys.* **2010**, *81*, 125415–125420.
- (21) Schnadt, J.; Bruhwiler, P. A.; Patthey, L.; O’Shea, J. N.; Sodergren, S.; Odelius, M.; Ahuja, R.; Karis, O.; Bassler, M.; Persson, P.; et al. *Nature* **2002**, *418*, 620–623.
- (22) Sundararaman, R.; Narang, P.; Jermy, A. S.; Goddard, W. A.; Atwater, H. A. *Nat. Commun.* **2014**, *5*, 5788.
- (23) Ma, J.; Wang, Z.; Wang, L. W. *Nat. Commun.* **2015**, *6*, 10107.
- (24) Lu, Y. J.; Sokhoyan, R.; Cheng, W.-H.; Shirmanesh, G. K.; Davoyan, A. R.; Pala, R. A.; Thyagarajan, K.; Atwater, H. A. *Nat. Commun.* **2017**, *8*, 1631.
- (25) Brown, A. M.; Sundararaman, R.; Narang, P.; Goddard, W. A., III; Atwater, H. A. *ACS Nano* **2016**, *10*, 957–966.
- (26) Zhang, J.; Hong, H.; Zhang, J.; Fu, H.; You, P.; Lischner, J.; Liu, K.; Kaxiras, E.; Meng, S. *Nano Lett.* **2018**, *18*, 6057–6063.
- (27) Shin, H. J.; Hwang, I. W.; Hwang, Y. N.; Kim, D.; Han, S. H.; Lee, J. S.; Cho, G. *J. Phys. Chem. B* **2003**, *107*, 4699–4704.
- (28) Busby, M.; Chiorboli, C.; Scandola, F. *J. Phys. Chem. B* **2006**, *110*, 6020–6026.
- (29) Long, R.; Prezhdo, O. V. *J. Am. Chem. Soc.* **2011**, *133*, 19240–19249.
- (30) Long, R.; English, N. J.; Prezhdo, O. V. *J. Am. Chem. Soc.* **2012**, *134*, 14238–14248.
- (31) Ranno, L.; Dal Forno, S.; Lischner, J. *npj Comp. Mater.* **2018**, *4* (1), 31.
- (32) Zhang, Z.; Liu, L.; Fang, W. H.; Long, R.; Tokina, M. V.; Prezhdo, O. V. *Chem.* **2018**, *4* (5), 1112–1127.
- (33) Li, L.; Kanai, Y. *Chem.* **2018**, *4*, 937–939.
- (34) Long, R.; Prezhdo, O. V. *J. Am. Chem. Soc.* **2014**, *136*, 4343–4354.
- (35) Tully, J. C. *J. Chem. Phys.* **1990**, *93*, 1061–1071.
- (36) Craig, C. F.; Duncan, W. R.; Prezhdo, O. V. *Phys. Rev. Lett.* **2005**, *95*, 163001–163004.
- (37) Fischer, S. A.; Habenicht, B. F.; Madrid, A. B.; Duncan, W. R.; Prezhdo, O. V. *J. Chem. Phys.* **2011**, *134*, 024102–024111.
- (38) Burdick, W. R.; Saad, Y.; Kronik, L.; Vasiliev, I.; Jain, M.; Chelikowsky, J. R. *Comput. Phys. Commun.* **2003**, *156*, 22–42.
- (39) Parandekar, P. V.; Tully, J. C. *J. Chem. Phys.* **2005**, *122*, 094102–094108.
- (40) Parandekar, P. V.; Tully, J. C. *J. Chem. Theory Comput.* **2006**, *2*, 229–235.
- (41) Wang, L. J.; Akimov, A.; Prezhdo, O. V. *J. Phys. Chem. Lett.* **2016**, *7*, 2100–2112.
- (42) Jaeger, H. M.; Fischer, S.; Prezhdo, O. V. *J. Chem. Phys.* **2012**, *137*, 545–559.
- (43) Wang, L. J.; Trivedi, D.; Prezhdo, O. V. *J. Chem. Theory Comput.* **2014**, *10*, 3598–3605.
- (44) Sifain, A. E.; Wang, L. J.; Prezhdo, O. V. *J. Chem. Phys.* **2016**, *144*, 211102–211106.
- (45) Wang, L. J.; Prezhdo, O. V. *J. Phys. Chem. Lett.* **2014**, *5*, 713–719.
- (46) Neukirch, A. J.; Guo, Z.; Prezhdo, O. V. *J. Phys. Chem. C* **2012**, *116*, 15034–15040.
- (47) Kilina, S. V.; Neukirch, A. J.; Habenicht, B. F.; Kilin, D. S.; Prezhdo, O. V. *Phys. Rev. Lett.* **2013**, *110*, 180404–180409.
- (48) Kohn, W.; Sham, L. J. *Phys. Rev.* **1965**, *140*, A1133–A1138.
- (49) Kresse, G.; Furthmüller, J. *Phys. Rev. B: Condens. Matter Mater. Phys.* **1996**, *54*, 11169–11186.
- (50) Kresse, G.; Hafner, J. *Phys. Rev. B: Condens. Matter Mater. Phys.* **1993**, *47*, 558–561.
- (51) Perdew, J. P.; Burke, K.; Ernzerhof, M. *Phys. Rev. Lett.* **1996**, *77*, 3865–3868.
- (52) Kresse, G.; Joubert, D. *Phys. Rev. B: Condens. Matter Mater. Phys.* **1999**, *59*, 1758–1775.
- (53) Dion, M.; Rydberg, H.; Schröder, E.; Langreth, D. C.; Lundqvist, B. I. V. *Phys. Rev. Lett.* **2004**, *92*, 246401.
- (54) Klimeš, J.; Bowler, D. R.; Michaelides, A. *Phys. Rev. B: Condens. Matter Mater. Phys.* **2011**, *83*, 19.
- (55) Klimeš, J.; Bowler, D. R.; Michaelides, A. *J. Phys.: Condens. Matter* **2010**, *22* (2), 022201.
- (56) Häkkinen, H.; Moseler, M.; Kostko, O.; Morgner, N.; Hoffmann, M. A.; Issendorff, B. v. *Phys. Rev. Lett.* **2004**, *93*, 093401.
- (57) Schooss, D.; Blom, M. N.; Parks, J. H.; Issendorff, B. v.; Haberland, H.; Kappes, M. M. *Nano Lett.* **2005**, *5*, 1972–1977.
- (58) Krukau, A. V.; Vydrov, O. A.; Izmaylov, A. F.; Scuseria, G. E. *J. Chem. Phys.* **2006**, *125*, 224106.
- (59) Li, L.; Long, R.; Bertolini, T.; Prezhdo, O. V. *Nano Lett.* **2017**, *17* (12), 7962–7967.
- (60) Zhou, K. G.; Withers, F.; Cao, Y.; Hu, S.; Yu, G.; Casiraghi, C. *ACS Nano* **2014**, *8*, 9914–9924.
- (61) Li, H.; Zhang, Q.; Yap, C. C. R.; Tay, B. K.; Edwin, T. H. T.; Olivier, A.; Baillargeat, D. *Adv. Funct. Mater.* **2012**, *22* (7), 1385–1390.